2012

Spatial dispersion in three-dimensional drawn magnetic metamaterials

Alessandro Tuniz
University of Sydney

Benjamin Pope
University of Sydney

Anna Wang
University of Sydney

Maryanne C. J Large
University of Sydney

Shaghik Atakaramians
University of Sydney

See next page for additional authors

Publication Details

Tuniz, A., Pope, B., Wang, A., Large, M. C. J., Atakaramians, S., Min, S., Pogson, E. M., Lewis, R. A., Bendavid, A., Argyros, A., Fleming, S. C. & Kuhlmey, B. T. (2012). Spatial dispersion in three-dimensional drawn magnetic metamaterials. Optics Express, 20 (11), 11924-11935.

Spatial dispersion in three-dimensional drawn magnetic metamaterials

Alessandro Tuniz,[1,*] Benjamin Pope,[1] Anna Wang,[1] Maryanne C. J. Large,[1] Shaghik Atakaramians,[1] Seong-Sik Min,[1] Elise M. Pogson,[2] Roger A. Lewis,[2] Avi Bendavid,[3] Alexander Argyros,[1] Simon C. Fleming,[1] and Boris T. Kuhlmey[1]

[1]*Institute of Photonics and Optical Science (IPOS), School of Physics, University of Sydney, NSW, 2006, Australia*
[2]*School of Engineering Physics, University of Wollongong, NSW, Australia*
[3] *Materials Science and Engineering, Commonwealth Scientific and Industrial Research Organization, PO Box 218 Lindfield, Sydney, NSW, 2070 Australia*
[*]*alessandro.tuniz@sydney.edu.au*

Abstract: We characterize spatial dispersion in longitudinally invariant drawn metamaterials with a magnetic response at terahertz frequencies, whereby a change in the angle of the incident field produces a shift in the resonant frequency. We present a simple analytical model to predict this shift. We also demonstrate that the spatial dispersion is eliminated by breaking the longitudinal invariance using laser ablation. The experimental results are in agreement with numerical simulations.

OCIS codes: (160.2290) Fiber materials; (160.3918) Metamaterials.

References and links

1. W. Cai and V. M. Shalaev, *Optical Metamaterials: Fundamentals and Applications* (Springer Verlag, 2009).
2. R. C. McPhedran, I. V. Shadrivov, B. T. Kuhlmey, and K. Y. S., "Metamaterials and metaoptics," NPG Asia Mater. **3**, 100–108 (2011).
3. D. Schurig, J. J. Mock, B. J. Justice, S. A. Cummer, J. B. Pendry, A. F. Starr, and D. R. Smith, "Metamaterial electromagnetic cloak at microwave frequencies," Science **314**, 977–980 (2006).
4. Z. Liu, H. Lee, Y. Xiong, C. Sun, and X. Zhang, "Far-field optical hyperlens magnifying sub-diffraction-limited objects," Science **315**, 1686 (2007).
5. V. M. Shalaev, "Optical negative-index metamaterials," J. Opt. Soc. Am. **1**, 41–48 (2007).
6. M. Choi, S. H. Lee, Y. Kim, S. B. Kang, J. Shin, M. H. Kwak, K. Y. Kang, Y. H. Lee, N. Park, and B. Min, "A terahertz metamaterial with unnaturally high refractive index," Nature **470**, 369–373 (2011).
7. N. I. Landy, S. Sajuyigbe, J. J. Mock, D. R. Smith, and W. J. Padilla, "Perfect metamaterial absorber," Phys. Rev. Lett. **100**, 207402 (2008).
8. I. V. Shadrivov, A. A. Zharov, and Y. S. Kivshar, "Second-harmonic generation in nonlinear left-handed metamaterials," J. Opt. Soc. Am. B **23**, 529–534 (2006).
9. I. V. Shadrivov, A. B. Kozyrev, D. W. van der Weide, and Y. S. Kivshar, "Nonlinear magnetic metamaterials," Opt. Express **16**, 20266–20271 (2008).
10. S. Zhang, Y.-S. Park, J. Li, X. Lu, W. Zhang, and X. Zhang, "Negative refractive index in chiral metamaterials," Phys. Rev. Lett. **102**, 023901 (2009).
11. A. Boltasseva and V. M. Shalaev, "Fabrication of optical negative-index metamaterials: Recent advances and outlook," Metamaterials **2**, 1–17 (2008).
12. C. M. Soukoulis and M. Wegener, "Past achievements and future challenges in the development of three-dimensional photonic metamaterials," Nat. Photonics **5**, 523–530 (2011).
13. J. K. Gansel, M. Thiel, S. M. Rill, M. Decker, K. Bade, S. Volker, G. Freymann, S. Linden, and M. Wegener, "Gold helix photonic metamaterial as broadband circular polarizer," Science **325**, 1513–1515 (2009).
14. X. G. Peralta, M. C. Wanke, C. L. Arrington, J. D. Williams, I. Brener, A. Strikwerda, R. D. Averitt, W. J. Padilla, E. Smirnova, and A. J. Taylor, "Large-area metamaterials on thin membranes for multilayer and curved applications at terahertz and higher frequencies," Appl. Phys. Lett. **94**, 161113 (2009).

15. M. Walther, A. Ortner, H. Meier, U. Loffelmann, P. J. Smith, and J. G. Korvink, "Terahertz metamaterials fabricated by inkjet printing," Appl. Phys. Lett. **95**, 251107–251107 (2009).
16. H. Kim, J. S. Melinger, A. Khachatrian, N. A. Charipar, R. C. Y. Auyeung, and A. Piqué, "Fabrication of terahertz metamaterials by laser printing," Opt. Lett. **35**, 4039–4041 (2010).
17. J. C. Knight, "Photonic crystal fibres," Nature **424**, 847–851 (2003).
18. A. Argyros, "Microstructured polymer optical fibers," J. Lightwave Technol. **27**, 1571–1579 (2009).
19. A. Tuniz, B. T. Kuhlmey, R. Lwin, A. Wang, J. Anthony, R. Leonhardt, and S. C. Fleming, "Drawn metamaterials with plasmonic response at terahertz frequencies," Appl. Phys. Lett. **96**, 191101 (2010).
20. A. Wang, A. Tuniz, P. G. Hunt, E. M. Pogson, R. A. Lewis, A. Bendavid, S. C. Fleming, B. T. Kuhlmey, and M. C. J. Large, "Fiber metamaterials with negative magnetic permeability in the terahertz," Opt. Mater. Express **1**, 115–120 (2011).
21. A. Tuniz, R. Lwin, A. Argyros, S. C. Fleming, E. M. Pogson, E. Constable, R. A. Lewis, and B. T. Kuhlmey, "Stacked-and-drawn metamaterials with magnetic resonances in the terahertz range," Opt. Express **19**, 16480–16490 (2011).
22. E. Badinter, A. Ioisher, E. Monaico, V. Postolache, and I. M. Tiginyanu, "Exceptional integration of metal or semimetal nanowires in human-hair-like glass fiber," Materials Lett. **64**, 1902–1904 (2010).
23. P. Halevi, *Spatial Dispersion in Solids and Plasmas* (North-Holland, 1992).
24. P. A. Belov, R. Marqués, S. I. Maslovski, I. S. Nefedov, M. Silveirinha, C. R. Simovski, and S. A. Tretyakov, "Strong spatial dispersion in wire media in the very large wavelength limit," Phys. Rev. B **67**, 113103 (2003).
25. P. Belov, Y. Hao, and S. Sudhakaran, "Subwavelength microwave imaging using an array of parallel conducting wires as a lens," Phys. Rev. B **73**, 033108 (2006).
26. J. B. Pendry, "Negative refraction makes a perfect lens," Phys. Rev. Lett. **85**, 3966–3969 (2000).
27. C. E. Kriegler, M. S. Rill, M. Thiel, E. Müller, S. Essig, A. Frölich, G. von Freymann, S. Linden, D. Gerthsen, H. Hahn, K. Busch, and M. Wegener, "Transition between corrugated metal films and split-ring-resonator arrays," Appl. Phys. B **96**, 749–755 (2009).
28. C. Menzel, T. Paul, C. Rockstuhl, T. Pertsch, S. Tretyakov, and F. Lederer, "Validity of effective material parameters for optical fishnet metamaterials," Phys. Rev. B **81**, 035320 (2010).
29. M. Silveirinha and P. Belov, "Spatial dispersion in lattices of split ring resonators with permeability near zero," Phys. Rev. B **77**, 233104 (2008).
30. P. W. Kolb, T. D. Corrigan, H. D. Drew, A. B. Sushkov, R. J. Phaneuf, A. Khanikaev, S. H. Mousavi, and G. Shvets, "Bianisotropy and spatial dispersion in highly anisotropic near-infrared resonator arrays," Opt. Express **18**, 24025–24036 (2010).
31. J. Pendry, A. Holden, D. Robbins, and W. Stewart, "Magnetism from conductors and enhanced nonlinear phenomena," IEEE Trans. Microw. Theory Tech. **47**, 2075–2084 (1999).
32. J. Anthony, R. Leonhardt, A. Argyros, and M. C. J. Large, "Characterization of a microstructured zeonex terahertz fiber," J. Opt. Soc. Am. B **28**, 1013–1018 (2011).
33. R. Singh, E. Smirnova, A. J. Taylor, J. F. O'Hara, and W. Zhang, "Optically thin terahertz metamaterials," Opt. Express **16**, 6537–6543 (2008).
34. D. Grischkowsky, S. Keiding, M. Van Exter, and C. Fattinger, "Far-infrared time-domain spectroscopy with terahertz beams of dielectrics and semiconductors," J. Opt. Soc. Am. B **7**, 2006–2015 (1990).
35. M. C. K. Wiltshire, J. B. Pendry, W. Williams, and J. V. Hajnal, "An effective medium description of 'swiss rolls', a magnetic metamaterial," J. Phys-Condens. Mat. **19**, 456216 (2007).
36. D. B. Melrose and R. C. McPhedran, *Electromagnetic Processes in Dispersive Media* (Cambridge University Press, 1991).
37. http://www.comsol.com.
38. A. W. Snyder and J. D. Love, *Optical Waveguide Theory* (Springer, 1983).
39. C. Menzel, R. Singh, C. Rockstuhl, W. Zhang, and F. Lederer, "Effective properties of terahertz double split-ring resonators at oblique incidence," J. Opt. Soc. Am. B **26**, B143–B147 (2009).
40. K. B. Alici and E. Ozbay, "Oblique response of a split-ring-resonator-based left-handed metamaterial slab," Opt. Lett. **34**, 2294–2296 (2009).

1. Introduction

Electromagnetic metamaterials attract much attention, because they provide the opportunity to access optical properties not found in nature, typically via structural arrangements of resonant metal-dielectric components on the sub-wavelength scale [1, 2]. A wide range of metamaterial devices with novel properties have so far been demonstrated, including electromagnetic cloaks [3], lenses that beat the diffraction limit [4], negative [5] or large [6] refractive index materials, perfect absorbers [7], nonlinear optical mirrors [8], as well as nonlinear [9] and chiral [10] metamaterials.

The fabrication of 3-dimensional metamaterials, especially at terahertz, infrared, and optical frequencies, remains challenging [11, 12]; lithographic or direct-laser writing [13] techniques are versatile, but produce at best centimeter-sized samples with few metamaterial layers; self-assembly of metallic clusters allows for large-volume metamaterial production, but only for limited geometries. To overcome such limitations, a number of techniques for mass-producing large-area flexible metamaterials have emerged [14], including inkjet [15] and laser printing [16] techniques, which however are limited to 2-dimensional samples.

Inspired by the procedure for producing optical fibers and photonic-crystal fibers [17, 18], fiber drawing has recently emerged as a simple means of inexpensively fabricating large quantities of 3-dimensional metamaterials [19–21]. A macroscopic (centimeter-sized) dielectric preform, containing metallic structures with features of the order of 1 mm, is assembled, then heated in a furnace while being stretched down into fiber form. During this process, the dielectric softens and the metal melts, such that the cross-section of the preform is preserved during stretching, and the original structure is scaled down by many orders of magnitude. This process has so far enabled the production of continuous metal wire arrays down to the micrometer [19] and nanometer [22] scale (tailoring of effective permittivity), as well as longitudinally invariant subwavelength magnetic resonators on the microscale [21] (tailoring of effective permeability).

It is well known however, that for longitudinally invariant metamaterials (e.g. infinite metal wires), the electromagnetic response becomes non-local, as charge transport along the fibers occurs on length scales comparable to or greater than the wavelength of electromagnetic radiation. In contrast, a local electromagnetic response implies that the displacement of charge occurs only in the point where the field is applied [23]. This is clearly not the case for longitudinally invariant metamaterials, because as soon as the wave vector of the incoming field has a non-zero component along the wires, there is a spatial variation of the fields and currents along the wires, on a scale that, regardless of the wavelength, is inevitably smaller than the infinitely long wires. The relevant electromagnetic tensor thus becomes non-local, i.e. the response at a given point depends on the response at another point, which is equivalent to the electric response tensor being spatially dispersive [23]. In longitudinally invariant metamaterials (e.g. infinite metal wires) this effect is therefore important even in the very large wavelength limit [24]. The homogenized permittivity and permeability tensors $\boldsymbol{\varepsilon}$ (and $\boldsymbol{\mu}$, as we discuss below) then become functions of both frequency and wave-vector $\mathbf{k}$, and in particular of propagation direction. In the context of drawn magnetic resonators, this could for example manifest as a shift in the resonance frequency for different angles of incidence. Whilst intrinsically spatially dispersive metamaterials can offer tremendous opportunities in applications such as sub-wavelength resolution [25], spatial dispersion is not always desirable. Particularly, spatial dispersion is unwanted when homogenous media with an angle-independent response are required, such as for cloaks [3] or perfect lenses [26].

Spatial dispersion has been well-understood in the context of *electric* responses of wire arrays [24], but to our knowledge has not yet been considered in longitudinally invariant resonators. For example, whereas the magnetic response of electrically connected and disconnected resonators in the mid-infrared was recently studied in some detail [27], there is no mention of the angle-dependence of such resonances. Spatially dispersive magnetic metamaterials have however been considered in the context of effective parameter retrieval of fishnet structures [28]. It has also been demonstrated that arrays of electrically disconnected split-ring resonators may exhibit spatial dispersion when their effective magnetic permeability is near-zero [29]. Experiments on spatial dispersion in resonator arrays showed shifts in resonance which were attributed to electric dipole coupling effects [30]. Our recent study on the properties of magnetic resonators in fiber form only considered fields at normal incidence [20].

In this paper, we experimentally and numerically characterize the resonant transmittance

properties of longitudinally invariant metamaterial fiber resonators as a function of incident angle, observing a significant shift in resonant frequency. We also provide a simple analytical theory that accounts for the observed spatial dispersion. Additionally, we extend our previous fabrication procedure, using laser-ablation to *break* the longitudinal invariance, effectively producing 3-dimensional patterned arrays of on-fiber resonators. We find that for such 3D (patterned) arrays, the resonance does not shift as a function of angle, in contrast to the longitudinally invariant (unpatterned) samples. Our results are in agreement with 3-dimensional finite element simulations.

2. Unpatterned metamaterial fibers

2.1. Fabrication and measurements

Magnetic metamaterials at terahertz frequencies are commonly assembled from subwavelength metallic split ring resonators (SRRs), composed of a planar open conductive loops possessing an inductance L and a capacitance C, where the magnetic response is strongly varying near the LC resonance [31]. Previously, we presented a fabrication strategy for producing on-fiber slotted resonators, which are SRRs that are invariant along the longitudinal axis [20]. The fabrication procedure for such samples is presented in Ref. [20], and is illustrated schematically in Fig. 1(a)-1(e): a 2×2 cm^2 square preform of Zeonex polymer [32], chosen for its low absorption properties at terahertz frequencies, is drawn to fiber with 100 μm width, spooled onto a cylinder, and loaded onto a DC magnetron sputtering deposition system, where a $\sim$ 250 nm silver coating is applied on three sides to form square U-shaped resonators. Note that the metal thickness is larger than the skin depth of silver between $0.1-1$ THz, to ensure a strong

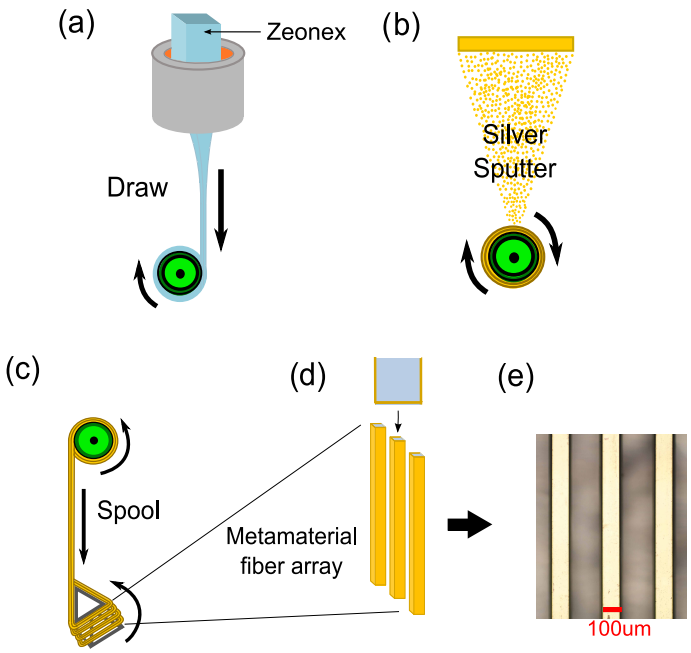

Fig. 1. Schematic of the fabrication procedure. (a) A Zeonex preform is fed through a furnace and drawn, (b) sputtered with silver on three sides and (c) spooled into an array. (d) Each side of the array forms a longitudinally invariant U-shaped resonator. (e) Optical microscope image of the 100 μm square fiber array (top view).

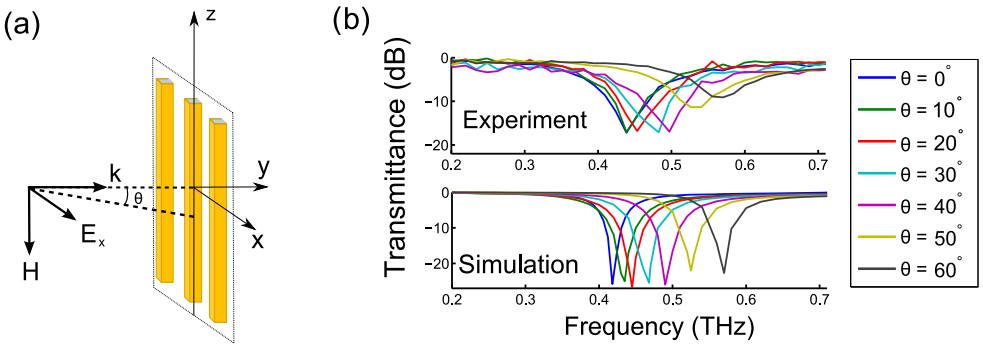

Fig. 2. (a) Schematic of the transmittance experiment under TM polarization (electric field directed perpendicular to the fibers) for different incident angles. (b) Experimental and numerical spectral transmittance for different angles of incidence.

magnetic resonance [20, 33]. This fiber is then re-spooled to produce a single flat metamaterial fiber array, supported in a frame of area 3×3 cm^2.

We experimentally characterized the transmittance of our samples using terahertz time-domain spectroscopy [34]. The transmission of electromagnetic field pulses was measured in the time domain for the array of resonators. The spectral amplitude of the transmitted field in the range $0.2 - 1$ THz was then calculated through a Fourier transform. The transmittance was obtained by dividing the intensity (field magnitude squared) of the transmission through the sample by that of a reference scan without the sample.

We measured the transmittance for our samples under TM polarization (electric field perpendicular to the fibers) for different angles of incidence θ, which is the angle of the **k**-vector with respect to the *y* propagation axis, as shown in the schematic of Fig. 2(a). In practice, the sample was rotated around the *x*-axis by an angle θ with respect to the *z* axis. The results are shown in Fig. 2(b). Dips in transmission are associated with a strong magnetic resonance and thus strong variations in the effective magnetic response [20]. We observe that the resonant frequency increases as the angle increases, a consequence of spatial dispersion.

In the case of metamaterials made from longitudinally invariant SRRs, the effect of the inductive-capacitive resonance at normal incidence can be interpreted as a strongly frequency dependent effective magnetic permeability [31, 35] around the resonant frequency, which can in particular yield negative retrieved effective permeability near the resonance [20]. A shift in the observed resonant frequency under different illumination angles indicates the effective permittivity is angle dependent, or in other words $\boldsymbol{\mu}$ depends on **k** at a given frequency and is thus spatially dispersive. However, when taking into account spatial dispersion, the distinction between electric and magnetic responses becomes arbitrary, and defining both a **k**-dependent permittivity and permeability is, in fact, redundant [36]. Instead, the entire electromagnetic response can be described by a spatially dispersive permittivity tensor and unity magnetic permeability, by *defining* the magnetization to be zero. Magnetic effects are then seen as higher order multipole moments of a **k**-dependent polarization field. While using such a re-definition avoids redundancy in the use of permittivity and permeability, it creates a disconnect with the spatially non-dispersive case. Alternative descriptions are equally valid [36]; in particular, by redefining the magnetization, both **k**-dependent permittivity and permeability can be used, although the separation is not unique and depends on the definition of the magnetisation. In the spatially dispersive case, there is thus some difficulty to unambiguously define - and identify - a magnetic response. Here, we circumvent this problem of definition by identifying the magnetic

response through the LC-resonance of the SRR resonators. The LC resonance is accompanied by what is unambiguously identified as a magnetic response. If the resonant frequency changes with **k**, then so does the magnetic response - whether the magnetic response is expressed in terms of a **k**-dependent permittivity or permeability tensors. This spatial dispersion of the magnetic response is due to the (non-local) induced charge transport along the metal, on a scale larger than the wavelength, and is a characteristic property of infinitely long structures. Other sub-wavelength magnetically responsive longitudinally invariant metamaterials, for example composed of "Swiss roll" metamaterials [35], would present the same effect.

To understand this phenomenon, we first model our fiber arrays using a full 3-dimensional finite element method [37], and obtain transmittance from scattering matrix parameters; we simulated a 100 μm square Zeonex fiber, coated by 1 μm of silver on three sides, included in a 300 μm-wide unit cell with Floquet boundary conditions to account for periodicity and changes in the incident angle. The silver film thickness of 1 μm, rather than 250 nm, was chosen to reduce computational cost, with little impact on results as both thicknesses are above the skin depth. We verified the validity of this approximation through selected simulations with 250 nm thickness (not shown). The simulation results, presented in Fig. 2(b), are in good agreement with experiment. The experimental resonances appear to be broader and weaker, especially at larger angles, which could be due to slight divergence in our beam (i.e. the beam is not perfectly collimated); this implies that, for a given θ, the electromagnetic field actually is incident over a (narrow) range of angles around θ, each corresponding to slightly different resonant frequency, thus broadening the transmission dip.

2.2. Theory and interpretation

The shift in resonance with increasing incident angle θ for the longitudinally invariant resonator case can be explained from Maxwell's equations and the geometrical invariance along the fibers. We assume for now that a single longitudinally invariant metallic resonator is embedded in a uniform dielectric with refractive index n everywhere outside the metal. The transmission dip is due to the coupling between an incoming plane wave of angular frequency ω and the resonant mode of the longitudinally invariant resonator with effective index n_{eff} and propagation constant $\beta = n_{\text{eff}}\omega/c$, which occurs when their phases are matched along z,

$$\beta = \frac{n\omega}{c}\sin(\theta), \tag{1}$$

where θ is the angle of incidence [see Fig. 2(a)], and c is the speed of light in vacuum. Due to the translational invariance of the structure along z, the electric field distribution of the resonant mode $\mathbf{E}_m(x,y)$ is a solution to the Helmholtz equation [38]

$$\nabla_t^2\mathbf{E}_m + \gamma\mathbf{E}_m = 0. \tag{2}$$

Here ∇_t^2 is the transverse Laplacian operator, and we have defined

$$\gamma = \left(\frac{n^2\omega^2}{c^2} - \beta^2\right). \tag{3}$$

Assuming the metal is a perfect electric conductor, so that $\mathbf{E} = 0$ at the metal, a mode is given by a solution to Eq. (2) satisfying $\mathbf{E} = 0$ at the resonator boundary. This is true independently of ω and β, so that if a field distribution $\mathbf{E}_m$ satisfies Eq. (2) and the boundary conditions set by the resonator for a given value of γ, this field distribution will define a resonant mode for all combinations of ω and β yielding the same value of γ through Eq. (3). The same resonant mode thus exists for all combinations of ω and β leaving γ unchanged. A resonance at normal incidence at frequency ω_0 corresponds to the coupling to a mode with $\beta = 0$, and thus $\gamma =$

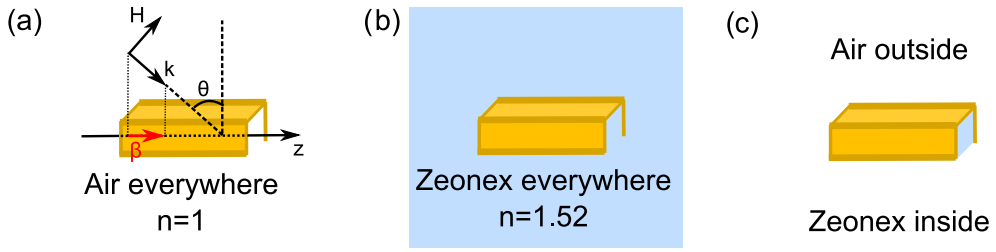

Fig. 3. Schematic of longitudinally invariant square resonators with (a) air everywhere, (b) Zeonex everywhere, (c) Zeonex inside the resonator, air outside the resonator. Note that (a) includes the relevant parameters: the wave-vector **k** forms an angle θ with respect to the normal of the longitudinal z axis of the resonators as shown, and phase-matches along z with the propagation constant β of the resonant mode. Only the magnetic field H is shown for clarity.

$n^2\omega_0^2/c^2$. The same resonance will exist for other values of β and ω having the same value of γ through Eq. (3), to which waves with an incident angle θ given by Eq. (1) can couple. Combining Eq. (1) and Eq. (3) then yields the frequency of the resonant mode as a function of incident angle:

$$\omega(\theta) = \frac{\omega_0}{\sqrt{1-\sin^2\theta}}. \tag{4}$$

To verify this theory, we calculated the transmittance under TM polarization as a function of angle for the square U-shaped resonators via the 3D finite-element model described in Section 2.1, but with either a refractive index of air ($n_{\text{air}} = 1$) or Zeonex ($n_{\text{znx}} = 1.52$) everywhere outside the metal, as shown in the schematics of Figs. 3(a)-3(b). We take the resonant frequency to be at the minimum of the resonant transmission dip, and tabulate how the resonance varies as a function of incident angle. Due to the computationally intensive nature of 3-dimensional finite element simulations, only the resonant frequency at normal incidence was calculated with a precision of 0.001 THz, whereas for all other angles the precision is 0.01 THz. The results are

Table 1. Theoretical and numerical resonance frequencies as a function of angle for different uniform dielectric refractive index values. For the theory columns, the value of ω_0 is taken from simulations at normal incidence.

	Resonant Frequency (THz) Air ($n = 1$)		Resonant Frequency (THz) Zeonex ($n = 1.52$)	
Incident angle θ	Simulation	Theory [Eq. (4)]	Simulation	Theory [Eq. (4)]
0°	0.564	-	0.372	-
10°	0.57	0.57	0.38	0.38
20°	0.60	0.60	0.40	0.40
30°	0.65	0.65	0.43	0.43
40°	0.73	0.74	0.49	0.49
50°	0.88	0.88	0.58	0.58
60°	1.13	1.13	0.74	0.74
70°	1.65	1.65	1.09	1.09
80°	3.25	3.25	2.13	2.14

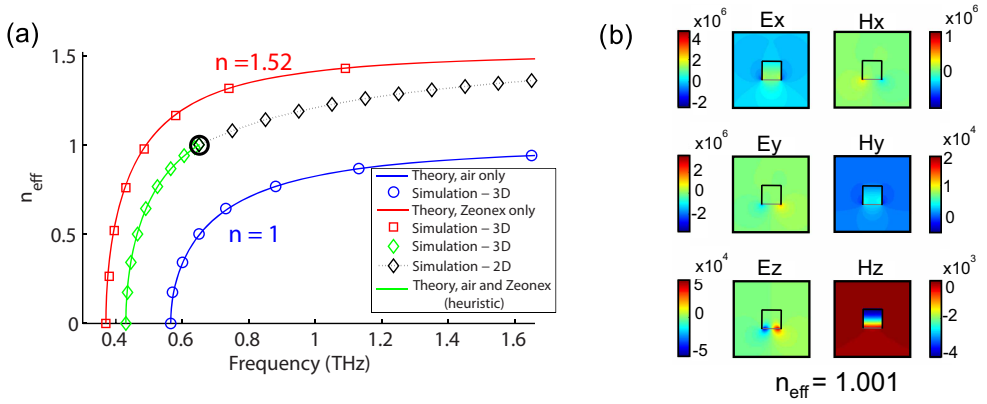

Fig. 4. (a) Calculated frequency-dependent effective index for structures in a uniform dielectric and for our fabricated structures. (b) Color density plot for the fields of the resonant mode, $n_{\text{eff}} = 1.001$ at 0.65THz.

shown in Table 1, and show excellent agreement with Eq. (4).

The refractive index distribution for our fabricated resonators, however, is non-uniform; Zeonex is in the center and air is in the surroundings, as shown in Fig. 3(c), requiring us to extend this analysis. Let us now consider the modes of the longitudinally invariant resonators as a function of frequency in terms of effective index n_{eff}, in the two limiting cases where the metal is embedded uniformly in air and uniformly in Zeonex. In this case, once the resonant frequency at normal incidence is known, one can obtain the resonant frequency as a function of angle θ via Eq. (4) (as already done in Table 1), and the corresponding effective index via Eq. (1). Figure 4(a) shows n_{eff} as a function of frequency for these two cases (blue and red data for air and Zeonex, respectively) obtained from the theory and 3D numerical results shown in Table 1.

On the same plot, we include the calculated frequency-dependent effective index of the fabricated structures. In this case, the data for $n_{\text{eff}} < 1$ (green diamonds) is obtained from the 3D simulations of Fig. 2(b) in combination with Eq. (1). For $n_{\text{eff}} > 1$ (black diamonds) the resonant modes cannot be excited from sideways incidence in free space; in this case the effective index is obtained by numerically solving for the propagation constant as a function of frequency using a finite element 2D eigenvalue solver [37] for a single resonator, from which the resonant mode can be identified. Figure 4(b) shows a close-up color density plot of the electric and magnetic field components at resonance with $n_{\text{eff}} = 1.001$ at 0.65 THz, circled in black in Fig. 4(a). Note that for the case where the effective index of the resonant structure is smaller than the background, the 2D eigenvalue method is not suitable due to coupling between the radiative resonant modes and free-space modes, thus rendering the unequivocal identification of the resonant mode difficult. However for $n_{\text{eff}} > 1$ a unique resonant bound mode is found in each case, independently of the simulation boundary, provided the boundary is large enough that the fields decay there. Both approaches coincide as $n_{\text{eff}} \to 1$.

The green/black curves in Fig. 4(a) suggest that the effective index of our fabricated structures behaves like that of a resonator included in a uniform background with a refractive index $\tilde{n}$ that lies between air and Zeonex, i.e. $1 < \tilde{n} < 1.52$. Re-writing Eq. (3) as

$$\gamma = \left(\frac{\tilde{n}^2 \omega^2}{c^2} - \beta^2 \right), \tag{5}$$

and following our previous reasoning, we obtain the wavelength dependence of the resonance

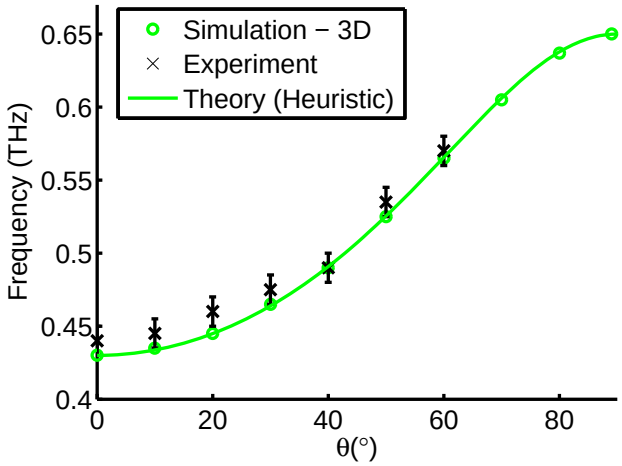

Fig. 5. Measured resonant angle, compared to the simulation, for the longitudinally invariant samples. The change in resonant frequency with respect to incident angle is well predicted by the heuristic theory.

frequency as a function of incident angle, using the phase matching condition of Eq. (1) with air outside the resonators:

$$\omega(\theta) = \frac{\omega_0}{\sqrt{1-\sin^2\theta/\tilde{n}^2}}. \tag{6}$$

In principle, the value of $\tilde{n}$ can be obtained from perturbation theory: to obtain $\tilde{n}$ one can consider the resonant mode of the fabricated structures (air outside the resonators, Zeonex inside the resonators) to be a perturbation to the uniform background case (air everywhere, noting that the same result is obtained starting from Zeonex everywhere); this is presented in detail in the Appendix. While this method gives an explicit formula for $\tilde{n}$ and justifies Eq. (6), the procedure fails in our particular configuration. The perturbations are not weak, in that the refractive index difference between air and Zeonex is strong in regions where the field intensities are large [Fig. 4(b)], since the Zeonex/air boundary is in the immediate vicinity of the resonator. Additionally, the fraction of power inside the resonator is frequency dependent, so that no unique value of $\tilde{n}$ can be defined to first order [see Eq. (11) in the Appendix], and a higher order perturbation would need to be used. Instead, we note that Eq. (6) only has two parameters: the resonance at normal incidence, which we calculate from a simple 2D simulation ($\omega_0 = 2\pi \times 0.43$ THz at $\theta = 0°$), and the value of $\tilde{n}$, which can be obtained from the resonant frequency at cutoff ($n_{\text{eff}} = 1$ at $\omega' = 2\pi \times 0.65$ THz at $\theta = 90°$):

$$\tilde{n} = \sqrt{\frac{1}{1-\omega_0^2/\omega'^2}} = 1.33. \tag{7}$$

The green curve in Fig. 4 shows the effective index obtained using this heuristic approach, and shows excellent overlap with the calculated data points.

Finally, we compare the *measured* angle-dependent resonant frequency [see Fig. 2(b)] of the fiber resonators with the numerical and theoretical results presented so far; all results are shown in Fig. 5, and are in good agreement.

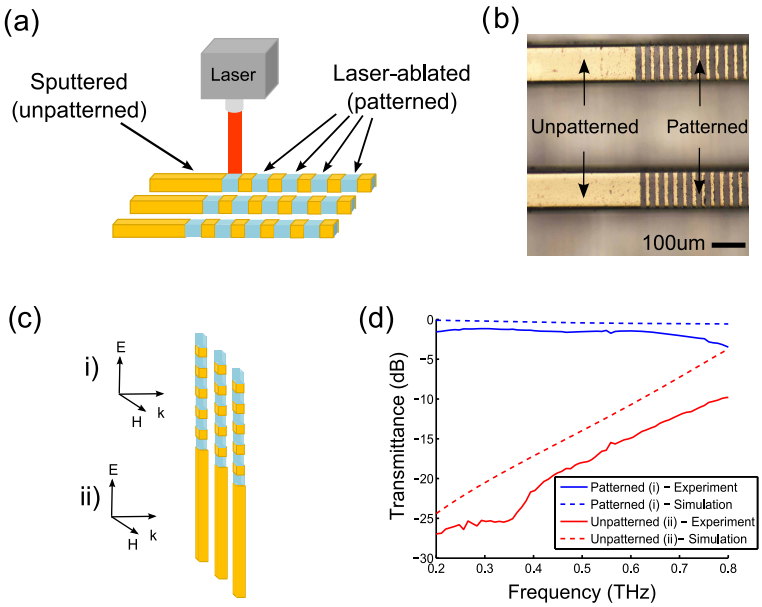

Fig. 6. (a) Schematic of the laser-ablation procedure, resulting in 3-dimensional (patterned) resonators from longitudinally invariant (unpatterned) resonators. (b) Optical microscope image of the patterned and unpatterned fibers. (c) The transmittance was measured for both i) the unpatterned and ii) the patterned region of the sample, for TE polarization (electric field directed along the fibers). (d) Experimentally measured and simulated transmittance.

3. Patterned metamaterial fibers: fabrication and characterization

In order to suppress the spatial dispersion, we used laser ablation to periodically remove $\sim 20\ \mu$m portions of the metal coating on the three sides, thus breaking the longitudinal invariance, as shown in the schematic of Fig. 6(a). We obtained arrays of 3-dimensional resonators with a width of 10 μm, patterned across a 5×5 mm^2 portion of the array. All features are thus much smaller than the resonant wavelength at every angle of incidence. A top-view optical microscope image of the resulting patterned and unpatterned portion of the samples is shown in Fig. 6(b).

To ensure that the patterning procedure was successful, we first measured the transmittance under TE polarization (electric field directed along the fibers). Appropriate lenses allowed to focus the field down to a spot size of approximately 1 mm, allowing us to selectively measure the transmitted field either through the unpatterned or the patterned portion of the sample [Fig. 6(c)]. The results are shown in Fig. 6(d). Note that for the unpatterned portion of the sample, the array behaves like a high-pass filter due to the electric currents induced in the metal by the electric field, which is typical of sub-wavelength metallic gratings [1, 19, 20]. In contrast, the electric field is transmitted in the patterned portion of the sample, confirming that our fibers have been ablated on three sides, and that the resonators are electrically disconnected from each other. The transmission curves are in agreement with the finite element calculations (dashed lines), the details of which were presented in Section 2.

We characterized the transmittance under TM polarization for different illumination angles θ with respect to the y propagation axis [Fig. 7(a)]. The results are shown in Fig. 7(b). In this case, the resonant frequency remains unchanged as the angle increases, in agreement with other

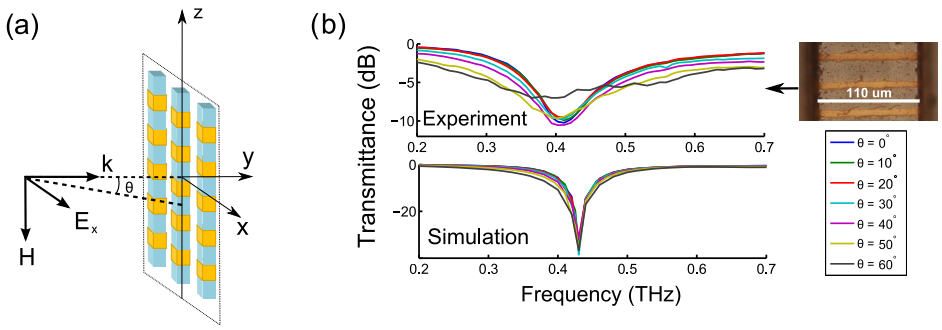

Fig. 7. (a) Schematic of the transmittance experiment under TM polarization (electric field directed perpendicular to the patterned fibers) for different incident angles. (b) Experimental and numerical spectral transmittance for different angles of incidence. Note that in this case the fiber is ~ 110 μm wide.

oblique-incidence transmittance studies in split-ring resonators [39, 40], but in contrast to our previous measurement for unpatterned resonators. Note that there is a slight difference in the resonant frequency for this portion of the sample compared to simulation; in this particular array, the square fiber is ~ 110 μm wide (inset), which leads to a decrease in LC resonance at 0.41 THz. In the numerical modeling, we have kept a square fiber with a 100 μm width, and the resonance at 0.43 THz is the same as for the unpatterned case. Though there is a difference in the resonance depth, possibly due to the edge imperfections and roughness induced by the laser ablation, both simulation and experiment clearly demonstrate that 3D patterning successfully suppresses spatial dispersion.

4. Conclusion

In conclusion, we characterized the transmittance at oblique incidence of longitudinally invariant metamaterial fiber arrays, produced by coating square fibers with metal. We found a strong dependence of resonant frequency on the incident angle due to spatial dispersion. We showed that a simple model based on the longitudinal invariance and the Helmholtz equation predicts the shift in resonance as a function of angle for the unpatterned samples, fitting both experimental and numerical data well. To eliminate spatial dispersion, we produced 3-dimensionally patterned U-shaped resonators via laser ablation, breaking their longitudinal invariance and resulting in an angle-independent resonant response. Having identified the longitudinal invariance as the cause of the spatial dispersion, we have thus demonstrated that it can be overcome by patterning the longitudinally-invariant fiber resonators, which will play a key role in the design of fiber-based metamaterial devices.

Appendix

If $\mathbf{E}(x,y)$ and $\mathbf{H}(x,y)$ are the electric and magnetic field mode profiles with effective index n_{eff} of a structure with a refractive index distribution $n(x,y)$, and $\overline{\mathbf{E}}(x,y)$ and $\overline{\mathbf{H}}(x,y)$ are the field mode profiles with effective index $\overline{n}_{\text{eff}}$ of a structure with refractive index distribution $\overline{n}(x,y)$, the difference in propagation constants at a given frequency is given by [38]

$$\delta n = n_{\text{eff}} - \overline{n}_{\text{eff}} = \frac{\int_{A_\infty} (n^2 - \overline{n}^2)\mathbf{E}\cdot\overline{\mathbf{E}}^*\,\mathrm{d}A}{Z_0 \int_{A_\infty} \left(\mathbf{E}\times\overline{\mathbf{H}}^* + \overline{\mathbf{E}}^*\times\mathbf{H}\right)\cdot\hat{\mathbf{z}}\,\mathrm{d}A}, \tag{8}$$

where Z_0 is the impedance of free space, and the integral is performed over the entire domain area A_∞. We consider the actual structure (with modal fields $\overline{\mathbf{E}}$ and $\overline{\mathbf{H}}$ and effective index $\overline{n}_{\text{eff}}$) to be a perturbation of the metallic resonator embedded in air only (with modal fields $\mathbf{E}$ and $\mathbf{H}$ and effective index $n_{\text{eff}}^{\text{air}}$). The effective index $\overline{n}_{\text{eff}}$ of the perturbed structure, to first order ($\mathbf{E} = \overline{\mathbf{E}}$ and $\mathbf{H} = \overline{\mathbf{H}}$) is then

$$\overline{n}_{\text{eff}} = n_{\text{eff}}^{\text{air}} + \frac{\int_{A_\infty} \left[\overline{n}(x,y)^2 - 1\right] |\mathbf{E}|^2 \, \mathrm{d}A}{2Z_0 \int_{A_\infty} \Re\mathrm{e}\,(\mathbf{E} \times \mathbf{H}^*) \cdot \hat{\mathbf{z}} \, \mathrm{dA}}, \tag{9}$$

where $\overline{n}(x,y)$ is the refractive index distribution of the full structure, i.e. $n_{\text{znx}} = 1.52$ on the inside of the metallic resonator, and $n_{\text{air}} = 1$ outside. A hypothetical structure with constant refractive index $\tilde{n}$ inside and out of the resonator, considered as a perturbation of the resonator embedded in air only, would have to first order

$$n'_{\text{eff}} = n_{\text{eff}}^{\text{air}} + \frac{\int_{A_\infty} \left[\tilde{n}^2 - 1\right] |\mathbf{E}|^2 \, \mathrm{d}A}{2Z_0 \int_{A_\infty} \Re\mathrm{e}\,(\mathbf{E} \times \mathbf{H}^*) \cdot \hat{\mathbf{z}} \, \mathrm{dA}}. \tag{10}$$

Equating the two expressions for n'_{eff} and $\overline{n}_{\text{eff}}$ we obtain an expression that $\tilde{n}$ must satisfy

$$\tilde{n} = \sqrt{1 + (n_{\text{znx}}^2 - 1)\, f}, \tag{11}$$

where f is the fraction of power inside the resonator.

Acknowledgments

This research was supported by the Australian Research Council under the Discovery Project scheme number DP120103942. B.T.K. and A.A. acknowledge support from an Australian Research Council Future Fellowship and Australian Research Fellowship, respectively. This work was performed in part at the Optofab node of the Australian National Fabrication Facility (ANFF) using Commonwealth and NSW State Government funding. ANFF was established under the National Collaborative Research Infrastructure Strategy to provide nano- and microfabrication facilities for Australia's researchers. The work at the University of Wollongong was supported by the Australian Research Council. This material is based on research sponsored by the Air Force Research Laboratory, under Agreement No. FA2386-11-1-4049. We thank Dr Richard Lwin at the University of Sydney for assistance in drawing the fiber and Dr Benjamin Johnston at Macquarie University for assistance in laser-ablating the fiber.